Research Square

Preprints are preliminary reports that have not undergone peer review.
They should not be considered conclusive, used to inform clinical practice,
or referenced by the media as validated information.

Metastable $CeZrO_4$ polymorph for high-sensitivity nitrogen dioxide detection

Minghui Yang

myang@dlut.edu.cn

Dalian University of Technology https://orcid.org/0000-0003-1071-1327

Xichao Mo

Dalian University of Technology

Jiaxin Li

Dalian University of Technology

Fengge Liu

Department of Platform and Devices, Google LLC

Haoran Zhao

Guilin University of Technology

Jinyang Hu

Guilin University of Technology

Zhaorui Zhang

Dalian University of Technology

Chenshuai Han

Dalian University of Technology

Congling Yin

Guilin University of Technology https://orcid.org/0000-0002-5525-4345

Jianrong Zeng

Shanghai Advanced Research Institute https://orcid.org/0000-0003-4867-1893

J. Attfield

University of Edinburgh https://orcid.org/0000-0001-9763-3987

Article

Keywords: Metastable polymorph sensor, Electrochemical gas sensor, NO2 detection, CeZrO4 sensor, Gas-sensing phase engineering

Posted Date: January 27th, 2026

DOI: https://doi.org/10.21203/rs.3.rs-8587725/v1

License: This work is licensed under a Creative Commons Attribution 4.0 International License.
Read Full License

Additional Declarations: There is **NO** Competing Interest.

Abstract

Accurate, real-time detection of nitrogen dioxide (NO_2) is essential for enforcing next-generation vehicle emission standards and ensuring environmental safety. Electrochemical devices offer a cost-effective solution; however, current sensing materials have limited sensitivity, stability, and selectivity. Here, we report a metastable polymorph of $CeZrO_4$, stabilized by liquid-nitrogen quenching, as a high-performance NO_2-sensing material. The metastable tetragonal structure permits high concentrations of Ce^{3+} and oxygen vacancies, and has high-energy surfaces, which collectively facilitate NO_2 adsorption and charge transport. The resulting sensor achieves an unprecedented 24,000% current response to 10 ppm NO_2, compared to 3,300% for the equilibrium cubic phase and 3,050% for the best reported literature material, while maintaining stable operation under variable humidity and temperature. These findings demonstrate that metastable phases offer an effective route to tune sensing materials, and the current example provides a scalable platform for precise, durable, and sensitive NO_2 monitoring as required, e.g., in the Euro 7 emission framework.

Introduction

The rapid phase-out of conventional fuel vehicles under the European Green Deal has elevated nitrogen dioxide (NO_2) as a critical metric for emission compliance[1]. The newly enacted Euro 7 framework—Regulation (EU) 2024/1257 with Implementing Regulations (EU) 2025/1706/1707—retains light-duty NO_x limits of 60 mg·km^{-1} for positive ignition (PI) and 80 mg·km^{-1} for compression ignition (CI) vehicles, and requires on-board monitoring (OBM) to report tailpipe NO_x concentration and mass flow as 1-s averages updated at least once per second, enabling real-time, high-accuracy NO_2-capable sensing under dynamic driving conditions[2]. Although Euro 7 does not prescribe a formal minimum detectable NO_2 concentration in ppm, its NO_x limits correspond to tailpipe NO_2 levels of a few to tens of ppm under representative light-duty conditions. These regulatory requirements expose the inadequacies of existing technologies, which often fail to capture transient, low-concentration variations of NO_2 amid fluctuating temperature and humidity. Consequently, the development of reliable, selective, and durable sensors has become an essential technological priority for environmental surveillance, verifying emission compliance and enabling sustainable transportation[3–5].

Optical, metal–oxide–semiconductor (MOS), and electrochemical approaches are presently the leading applicable NO_2 detection technologies[6–8]. Optical techniques can deliver ppb-level precision and excellent selectivity; however, their bulky optics, high power consumption, and relatively high cost impede deployment in compact on-board platforms[9–11]. MOS sensors—typically based on WO_3, SnO_2, or In_2O_3—offer simple architectures but generally require elevated operating temperatures (often > 200–300°C) and suffer from cross-sensitivity and limited selectivity under real-world humidity and multi-gas backgrounds[12–14]. Electrochemical sensors enable low-temperature operation and miniaturization[15]; however, they are prone to humidity-induced drift, electrolyte dehydration/flooding, and electrode aging,

which together constrain long-term stability and quantitative accuracy[16]. Here we report that many of the latter demerits are overcome through use of a metastable $CeZrO_4$ polymorph, which delivers outstanding electrochemical sensing performance.

We demonstrate that metastable tetragonal $CeZrO_4$, stabilized via liquid-nitrogen quenching, serves as a highly active sensing material for electrochemical NO_2 detection. The metastable phase, characterized by enriched Ce^{3+} species, abundant oxygen vacancies, and high-energy exposed facets, promotes efficient NO_2 adsorption, rapid charge transport, and accelerated surface redox reactions. As a result, the corresponding sensor achieves an exceptional 24,000% current response to 10 ppm NO_2, eightfold higher than that of the equilibrium cubic counterpart, at room temperature. Beyond setting a new performance benchmark, this metastable-phase strategy provides a robust and scalable pathway to address the critical demand for accurate, durable, and humidity-tolerant NO_2 sensors mandated by Euro 7 emission regulations, establishing a direct bridge between metastable materials design and next-generation regulatory sensing technologies.

Results and discussion

Material Characterization and Metastable Polymorphs Stabilization

Polycrystalline $CeZrO_4$ was synthesized through a sol-gel route. Samples were preheated to 300, 600, or 900°C (labeled $CeZrO_4$-300, etc.) and quenched into liquid nitrogen (Video S1). Two control samples were obtained by slow furnace cooling ($CeZrO_4$-S) and natural air cooling ($CeZrO_4$-Q).

X-ray diffraction (XRD) reveals sample variations with quenching temperature (Figure S1), and Rietveld refinements using neutron powder diffraction (NPD) data confirm the coexistence of the stable cubic c-$CeZrO_4$ polymorph (space group Fm-3m) and a metastable tetragonal t-$CeZrO_4$ polymorph ($P4_2/nmc$) (Figure S2–S7, Table S1–S14)[17, 18]. The t-$CeZrO_4$ fraction has a maximum value of ~ 91% at 600°C as analysed by XRD. Consistently, NPD analysis yields a t-$CeZrO_4$ fraction of ~ 95%, further confirming the XRD results (Fig. 1a–c). In situ variable-temperature XRD (VT-XRD) further shows that kinetic arrest at 600°C maximizes the tetragonal phase, establishing rapid quenching as an effective route to stabilize this otherwise metastable configuration (Figure S8). Magnified VT-XRD patterns (Figure S9–S11) display distinct tetragonal reflections whose intensity maximizes at 600°C, in agreement with XRD and NPD refinements. These results unambiguously establish that kinetic arrest by rapid quenching effectively stabilizes the metastable tetragonal phase at this temperature.

Scanning electron microscopy (SEM) and transmission electron microscopy (TEM) show that quenching preserves the nanoblock morphology while simultaneously introducing surface roughness, lattice rearrangement, and concentric diffraction rings characteristic of polycrystalline materials (Figure S12, S13). Energy-dispersive X-ray spectroscopy (EDS) mapping verifies uniform elemental distribution

(Figure S14), and Brunauer-Emmett-Teller (BET) analysis shows negligible variation across all samples (Figure S15), indicating that the sensing enhancement shown later does not arise from changes in surface area.

X-ray photoelectron spectroscopy (XPS) and X-ray absorption fine structure (XAFS) analyses were performed to probe the electronic structure of as-prepared $CeZrO_4$ and quenched samples. The high-resolution Ce 3d spectra reveal coexisting Ce^{3+}/Ce^{4+} states, with $CeZrO_4$-600 showing a clear shift toward lower binding energy and the highest Ce^{3+} fraction (Fig. 1d, S16-S18; Table S15). This shift reflects oxygen-vacancy formation at the surface, which modulates the local electronic environment and underpins improved redox activity[19, 20]. O 1s spectra further show that $CeZrO_4$-600 contains a significantly higher fraction of oxygen vacancies and chemisorbed oxygen, with the adsorbed oxygen component increasing from 1.75% to 17.55% (Fig. 1e). This enrichment of surface-active oxygen species is consistent with the increased Ce^{3+} population. Ce L_3-edge X-ray absorption near-edge structure (XANES) of $CeZrO_4$-600 displays a subtle edge shift to lower energy, corroborating its higher Ce^{3+} population (Fig. 1f, S19)[21, 22]. In contrast, Zr K-edge spectra remain largely unchanged, though extended X-ray absorption fine structure (EXAFS) analysis reveals shorter Zr–O bond lengths and reduced Zr–Zr coordination intensity (Fig. 1g, h). Wavelet transform (WT) analysis further shows increased local disorder after quenching (Fig. 1i, S20), consistent with the cubic-to-tetragonal transition. Such lattice distortion plays a critical role in tuning the electronic structure, facilitating charge transport, and promoting surface reactions[23–25]. More broadly, these findings underscore lattice distortions and defect engineering as design principles for tailoring redox-active oxides toward advanced electrochemical functions.

Gas sensing properties

Electrochemical devices based on quenched $CeZrO_4$-600 exhibit the highest NO_2 response in the series (Fig. 2a–c, S21–S24). At 10 ppm, the relative current change reaches 24,000%, nearly eightfold higher than that of cubic $CeZrO_4$, with rapid response and recovery times of 7 s and 8 s, respectively. The sensor shows a linear detection range from 50 ppb to 10 ppm, with a sensitivity of 559 nA ppm^{-1}, more than three times higher than the unquenched sample (Inset of Fig. 2b). The $CeZrO_4$-600 sensor exhibits excellent long-term stability, retaining 98% of its initial response after 90 days (Fig. 2d). Stabilization of the metastable tetragonal polymorph is central to this performance gain over equilibrium phases. When employed as the sensing material in electrochemical gas sensors, it confers a distinct advantage over commonly studied semiconductor and electrochemical-based NO_2 sensors. Benchmarking against recent reports positions $CeZrO_4$-600 at the forefront of NO_2 detection, combining high sensitivity, robust selectivity, strong humidity tolerance, and long-term stability (Fig. 2e, Table S16). Moreover, its response remains nearly constant across a wide temperature range (− 25 to 75°C), with less than 15% variation in current, underscoring excellent thermal stability. This temperature insensitivity originates from the stable

Ce^{3+}/Ce^{4+} redox couple and efficient proton conduction sustained by Nafion, which together buffer thermal perturbations and maintain stable electrochemical kinetics (Fig. S25)[26].

Performance is highly reproducible across multiple cycles (Fig. 3a, S26), confirming that quenching at 600°C yields optimal sensing characteristics. The $CeZrO_4$-600 sensor delivers exceptional NO_2 selectivity against all tested interfering gases (Fig. 3b). It exhibits minimal variation (< 5 nA) under varying relative humidity (RH), thanks to a compact design with a sealed water reservoir that stabilizes internal humidity (Fig. 3d). This effectively eliminates humidity-induced interference, a common limitation in conventional sensors. While optical sensors offer slightly faster response and lower detection limits, they are limited by higher cost, larger size, and greater power consumption (Fig. 3c)[27]. $CeZrO_4$-600 achieves high performance across all practical metrics and at a low cost. By integrating key comprehensive factors—including cost, volume, and power—into a unified reference metric, its advantage becomes evident across the full spectrum of reported NO_2 sensors, spanning optical, mass, acoustic, and electrical platforms (Fig. 3e, Table S17 and S18). These results highlight that metastable-polymorph engineering not only enhances intrinsic sensor performance but also delivers a comprehensive, field-spanning advantage for next-generation NO_2 detection.

Gas sensing mechanism

UV–vis diffuse reflectance spectroscopy (DRS) shows only a minor bandgap change upon quenching ($\Delta Eg \approx 0.04$ eV, Figure S27), indicating that the enhanced sensing cannot be ascribed to bandgap modulation[28, 29]. Instead, in situ Fourier transform infrared spectroscopy (FTIR) reveals sequential $NO_2 \rightarrow NO_2^- \rightarrow NO$ transformations on $CeZrO_4$-600 (Fig. 4a, b), evidencing a surface-mediated redox pathway facilitated by abundant surface-active sites[15,30]. The The enhanced sensing thus originates from the surfaces of the metastable t-$CeZrO_4$ stabilized by rapid quenching. Its lower symmetry relative to c-$CeZrO_4$ induces lattice distortions and exposes high-energy facets, while the preserved Ce^{3+} population sustains abundant oxygen vacancies and adsorbed oxygen species. These features collectively promote NO_2 adsorption, accelerate charge transfer, and enhance surface-reaction kinetics. Density functional theory (DFT) calculations reveal stronger NO_2 binding on the t-$CeZrO_4$ surface than on c-$CeZrO_4$ (Figure S28, S29), with higher adsorption energy (− 3.38 vs − 1.09 eV) and greater electron transfer (0.132 e vs 0.064 e, Fig. 4c–g). Charge-density difference maps further show pronounced charge redistribution on the tetragonal phase, consistent with its enriched active sites. Together with experimental evidence, these insights underscore metastable polymorph stabilization as a general strategy for advancing electrochemical gas sensors. This mechanistic framework underscores the broader potential of metastable structures to reshape catalytic and sensing processes across diverse classes of materials.

Vehicle exhaust monitoring applications

To validate the relevance of the sensor under Euro 7 emission regulations, we conducted an on-road NO_2 monitoring test designed for compliance-oriented diagnostics. Conventional inspection and onboard systems, optimized for total NO_x evaluation, are inadequate for precise, real-time NO_2 detection under dynamic exhaust conditions—a challenge directly addressed by the $CeZrO_4$-600 sensor. The integrated sensing platform (Fig. 5a, 5b, S30, S31) featured a wireless module that enabled real-time NO_2 quantification across NO_2 concentrations of 0.1–10 ppm, achieving relative errors below 5% during calibration (Fig. 5c, S32). Selectivity measurements confirmed negligible interference from major exhaust components (Fig. 5d). Under controlled laboratory conditions (27°C, 50% RH), the system accurately quantified ~ 10 ppm NO_2 from collected exhaust samples (Fig. 5e). During transient engine operation (Video S2), the $CeZrO_4$-600 sensor precisely captured dynamic NO_2 fluctuations under moderate temperature (~ 35°C) and fluctuating humidity (~ 70% RH), demonstrating outstanding stability and robustness against real-world exhaust disturbances. Further real-vehicle testing across five consecutive ignition cycles revealed a reproducible transient NO_2 peak of approximately 15 ppm upon engine ignition, which rapidly decayed to steady-state levels (Fig. 5f). Even when the sensing distance was shortened to 5 cm from the exhaust outlet—creating harsher conditions with elevated temperature (43–55°C) and humidity (69–77% RH)—the sensor maintained accurate tracking of NO_2 fluctuations correlated with engine speed (rpm) (Fig. 5g, S33). The wireless sensing system exhibited outstanding performance, fulfilling not only the Euro 7 detection requirements but also the stricter China 6b standard[31]. To further improve signal quality, we applied a machine-learning (ML) denoising pipeline, which increased the signal-to-noise ratio (SNR) from 2.6 dB to 11 dB (Fig. 5h, S34–S38). Unlike traditional smoothing techniques, which often distort key transient features, this ML approach effectively suppressed environmental noise while preserving critical signal characteristics, enabling highly accurate NO_2 quantification. Such reliable, humidity-tolerant sensing performance under real exhaust dynamics directly addresses the core challenge of Euro 7 and real-driving emission (RDE) compliance, establishing metastable-polymorph $CeZrO_4$-600 as a technically mature and regulation-ready platform for next-generation NO_2 diagnostics. Collectively, these findings underscore metastable engineering as a powerful strategy to bridge materials innovation with real-world emission control.

Conclusion

In summary, this work demonstrates a metastable-phase strategy for advanced gas sensing through the stabilization of tetragonal $CeZrO_4$ via liquid-nitrogen quenching. The non-equilibrium structure, characterized by abundant oxygen vacancies, enhanced Ce^{3+} concentration, and high-energy facets, enables rapid NO_2 adsorption and electron transfer, leading to a record current response of 24,000% at 10 ppm. Compared with the equilibrium cubic counterpart, the metastable polymorph exhibits superior sensitivity, humidity tolerance, and operational durability. Beyond performance improvement, this approach establishes a versatile framework for engineering metastable systems with tailored charge dynamics. The study bridges materials thermodynamics with sensor design, offering a pathway toward

intelligent, regulation-ready sensing technologies for environmental monitoring and automotive emission control.

Methods

Preparation of pure-phase $CeZrO_4$

Pure-phase $CeZrO_4$ was synthesized via a modified sol–gel method. 0.01 mol of $Ce(NO_3)_3{\cdot}6H_2O$ and 0.01 mol of $Zr(NO_3)_4{\cdot}5H_2O$ were dissolved in 25 mL of deionized water under magnetic stirring. Subsequently, 0.02 mol of anhydrous citric acid was added as a complexing agent, and the mixture was stirred ultrasonically to ensure homogeneity. The solution was then heated to 120°C until it transformed into a yellow gel. This gel was vacuum-dried at 60°C for 10 h to remove residual water. The resulting dry gel was calcined in a muffle furnace at 900°C for 10 h with a heating rate of 10°C min^{-1}. The obtained pale-yellow powder was ground thoroughly and subjected to a second calcination under the same conditions to ensure phase purity.

Preparation of CeZrO- (x = 300, 600, 900) (liquid nitrogen–quenched samples)

To obtain samples containing the metastable t-$CeZrO_4$ phase, the as-prepared $CeZrO_4$ was placed in a ceramic crucible and heated to 300°C, 600°C, or 900°C in a muffle furnace. Once the target temperature was reached, the crucible was immediately removed and quenched in liquid nitrogen until complete evaporation occurred. The resulting samples were collected and labeled as $CeZrO_4$-300, $CeZrO_4$-600, and $CeZrO_4$-900, respectively. A detailed procedure is shown in Video S1.

Preparation of $CeZrO_4$-$_x$ (control samples)

For comparison, two control samples were prepared. In the first case, $CeZrO_4$ was heated to 600°C and then rapidly cooled in air by removing the crucible from the furnace. This sample was designated as $CeZrO_4$-Q (quenched in air). In the second case, $CeZrO_4$ was heated to 600°C and allowed to cool naturally within the furnace, yielding a sample designated as $CeZrO_4$-S (slow-cooled).

Preparation of electrochemical gas sensor

To evaluate the gas-sensing capabilities of $CeZrO_4$-x (x = 300, 600, 900) materials subjected to rapid liquid nitrogen quenching, fuel cell-type electrochemical gas sensors were fabricated and systematically tested. Response/recovery times (t_{90}) were the times to reach 90% of the total change. The response current, ΔI, was defined as the difference between the current measured in air (I_1) and that upon exposure to NO_2(I_2):

$$\Delta I = I_2 - I_1$$

The sensing response was defined as the relative change in current, calculated as:

$$R = \frac{I_2 - I_1}{I_1} \times 100\%$$

The electrochemical gas sensor comprised a Nafion membrane, electrodes, carbon paper, and a water reservoir. The preparation method is as follows: First, 10 mg of sample powder, 20 μL of 5% Nafion solution, and 200 μL of isopropyl alcohol were subjected to ultrasonic treatment for 20 min to obtain a dispersed material solution. The solution was then dropped onto two pieces of carbon paper using a burette. A polytetrafluoroethylene (PTFE) film served as the protective layer while the carbon paper with Nafion underwent treatment at 90°C and under pressure (1 MPa) for 90 s to form the sensitive material assembly. The Nafion membrane was pretreated as described in our previous work[15].

The use of carbon paper facilitates the uniform loading of sensitive materials onto both positive and negative electrodes. The sensitive material assembly is trimmed to a diameter of 1 cm and then combined with the electrodes using a hot melt adhesive, forming a compact fuel cell. Finally, a container filled with deionized water-soaked cotton is securely attached to the anode of the electrochemical gas sensor. During operation, the working electrode is exposed to the target gas, while the anode remains sealed within a container filled with humidified air.

Material characterization

Time-of-flight (TOF) neutron powder diffraction (NPD) data were collected on 2 g of $CeZrO_4$-600 using the General-Purpose Powder Diffractometer (GPPD) at the China Scattering Neutron Source (CSNS, Dongguan, China). The phase information and lattice parameters of prepared catalyst powders were characterized using X-ray diffraction (XRD, Rigaku MiniFlex 600 powder X-ray diffractometer with Cu Kα radiation at λ = 1.5418 Å, scanning speed: 0.1 °min^{-1}, 2θ range of 10–90°). To observe the surface morphology of the materials, scanning electron microscope (SEM) was used with JSM-7900F (Japan). The high-resolution transmission electron microscopy (HRTEM) images were acquired on a Talos JEM-F200 (Japan) instrument. X-ray photoelectron spectroscopy (XPS) was performed using a K-Alpha+ (USA) instrument. The binding energies of $CeZrO_4$ and $CeZrO_{4-x}$ (x = 300, 600, 900) surface were calibrated by C 1s peak (284.8 eV). The Ce L_3-edge and Zr K-edge X-ray absorption fine structure (XAFS) spectra were recorded using the easyXAFS 300 system (easyXAFS, US) in transmission mode. Brunauer-Emmett-Teller (BET) results of $CeZrO_4$ and $CeZrO_{4-x}$ (x = 300, 600, 900) were obtained by an automatic specific surface area and microporous pore analyzer (3FLEX, USA). UV–vis diffuse reflectance spectra (UV–vis–DRS) were measured using a UV-550 spectrophotometer. In situ infrared spectroscopy (in situ IR) was carried out using a VERTEX 70 spectrometer equipped with an MCT detector; all spectra were recorded by co-adding 32 scans at a resolution of 4 cm^{-1} over 4000 – 400 cm^{-1}.

Declarations

Conflict of Interest

The authors declare no competing interests.

Acknowledgements

This work was supported by the Young Scientists Fund (Class A) of the National Natural Science Foundation of China (Grant No. 22525102), the National Natural Science Foundation of China (Grant No. 62471085), the Fundamental Research Funds for the Central Universities (Grant Nos. DUT22RC(3)050, DUT24YG149, and DUT24YG109), the Programme of Introducing Talents of Discipline to Universities (Grant No. B13012), and the Engineering and Physical Sciences Research Council (EPSRC, UK). The authors acknowledge the assistance of the DUT Instrumental Analysis Center and beamline BL13SSW at Shanghai Synchrotron Radiation Facility for the XAFS.

Data Availability Statement

The data that support the findings of this study are available from the corresponding author upon reasonable request.

References

1. The European Green Deal, COM (2019) 640 final; https://eur-lex.europa.eu/legal-content/EN/TXT/?uri=CELEX:52019DC0640 (accessed 22 Nov 2025)
2. Official Journal of the European Union Commission Implementing Regulation (EU) 2025/1706 of 25 July 2025; https://eur-lex.europa.eu/legal-content/EN/TXT/?uri=CELEX:32025R1706 (accessed 22 Nov 2025).
3. Zhang H et al (2023) A chemiresistive-potentiometric multivariate sensor for discriminative gas detection. Nat Commun 14:3495
4. Modi A, Koratkar N, Lass E, Wei B, Ajayan PM (2003) Miniaturized gas ionization sensors using carbon nanotubes. Nature 424:171–174
5. Liu N, Tang ML, Hentschel M, Giessen H, Alivisatos AP (2011) Nanoantenna-enhanced gas sensing in a single tailored nanofocus. Nat Mater 10:631–636
6. Min H et al (2024) N-Carbon-Doped Binary Nanophase of Metal Oxide/Metal–Organic Framework for Extremely Sensitive and Selective Gas Response. Adv Mater 36:2309041
7. Sharma A et al (2024) Porous materials as effective chemiresistive gas sensors. Chem Soc Rev 53:2530–2577
8. Karhu J, Hieta T, Manoocheri F, Vainio M, Ikonen E (2021) LED-Based Photoacoustic NO_2 Sensor with a Sub-ppb Detection Limit. ACS Sens 6:3303–3307

9. Zhao P et al (2020) Mode-phase-difference photothermal spectroscopy for gas detection with an anti-resonant hollow-core optical fiber. Nat Commun 11:847
10. Wang Q et al (2022) Dual-comb photothermal spectroscopy. Nat Commun 13:2181
11. Wang Z et al (2024) Cavity-enhanced photoacoustic dual-comb spectroscopy. Light Sci Appl 13:11
12. Hu C et al (2025) Chemiresistive gas sensors for intelligent sensing: design strategies, emerging applications and future challenges. Chem Soc Rev 54:11302–11367
13. Jeong S-Y, Moon YK, Wang J, Lee J-H (2023) Exclusive detection of volatile aromatic hydrocarbons using bilayer oxide chemiresistors with catalytic overlayers. Nat Commun 14:233
14. Zhu L-Y et al (2023) Advances in Noble Metal-Decorated Metal Oxide Nanomaterials for Chemiresistive Gas Sensors: Overview. Nano Micro Lett 15:89
15. Mo X et al (2024) Nitrogen-Doped Indium Oxide Electrochemical Sensor for Stable and Selective NO_2 Detection. Adv Mater 36:2409294
16. Bulemo PM et al (2025) Selectivity in Chemiresistive Gas Sensors: Strategies and Challenges. Chem Rev 125:4111–4183
17. Zhu H et al (2018) Charge transfer drives anomalous phase transition in ceria. Nat Commun 9:5063
18. Quarti C et al (2016) Structural and optical properties of methylammonium lead iodide across the tetragonal to cubic phase transition: implications for perovskite solar cells. Energy Environ Sci 9:155–163
19. Hou W et al (2022) Catalytic Mechanism of Oxygen Vacancies in Perovskite Oxides for Lithium–Sulfur Batteries. Adv Mater 34:2202222
20. Li M-Y et al (2025) Unveiling the Intrinsic Superior SHG Performance of Ce^{4+} Fluoride Masked by Subtle Ce^{3+} Impurity and Its Effective Removal. Angew Chem Int Ed 64:e202502143
21. Hu H et al (2025) Engineered Nickel–Iron Nitride Electrocatalyst for Industrial-Scale Seawater Hydrogen Production. Adv Mater 37:2415421
22. Campbell CT, Peden CH (2005) F. Oxygen Vacancies and Catalysis on Ceria Surfaces. Science 309:713–714
23. Zeng L et al (2025) Quenching-induced lattice modifications endowing Li-rich layered cathodes with ultralow voltage decay and long life. Energy Environ Sci 18:284–299
24. Xia Z, Guo S (2019) Strain engineering of metal-based nanomaterials for energy electrocatalysis. Chem Soc Rev 48:3265–3278
25. Qin Y et al (2022) RuO_2 electronic structure and lattice strain dual engineering for enhanced acidic oxygen evolution reaction performance. Nat Commun 13:3784
26. Montini T, Melchionna M, Monai M, Fornasiero P (2016) Fundamentals and Catalytic Applications of CeO_2-Based Materials. Chem Rev 116:5987–6041
27. Womack CC et al (2022) A lightweight broadband cavity-enhanced spectrometer for NO2 measurement on uncrewed aerial vehicles. Atmos Meas Tech 15:6643–6652

28. Li Z, Yan T, Fang X (2023) Low-dimensional wide-bandgap semiconductors for UV photodetectors. Nat Rev Mater 8:587–603
29. Ning C-Z, Dou L, Yang P (2017) Bandgap engineering in semiconductor alloy nanomaterials with widely tunable compositions. Nat Rev Mater 2:17070
30. Zhao X et al (2025) Titanium nitride sensor for selective NO_2 detection. Nat Commun 16:182
31. Ministry of Environmental Protection of the People's Republic of China & General Administration of Quality Supervision, Inspection and Quarantine of the People's Republic of China. Limits and measurement methods for emissions from light-duty vehicles (CHINA 6) (GB 18352.6–2016) (in Chinese) (2016)

Figures

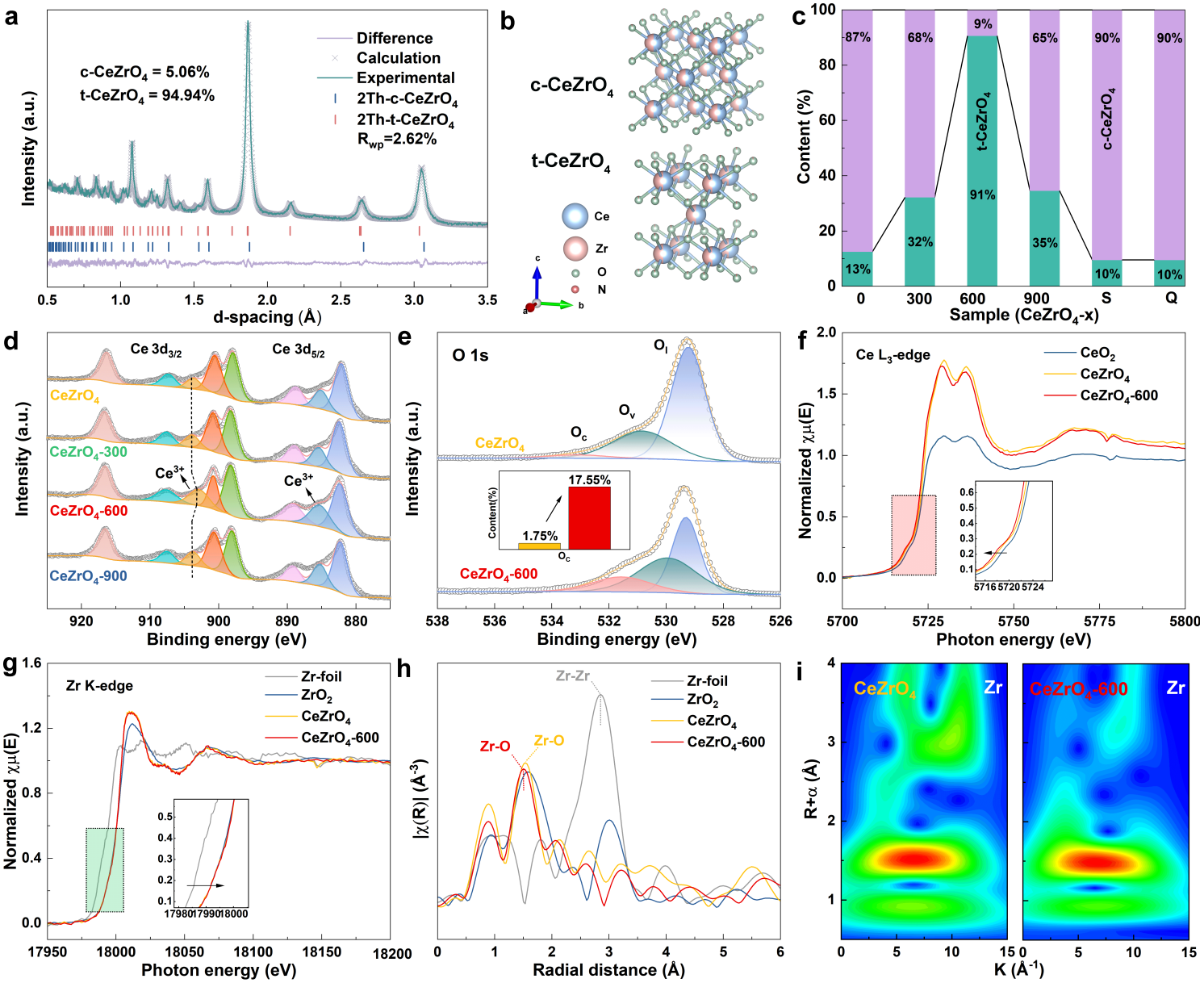


Figure 1

(a) Rietveld refinement plots of neutron powder diffraction (NPD) pattern for $CeZrO_4$-600. (b) Refined crystal structure of cubic c-$CeZrO_4$ polymorph (Fm-3m) and tetragonal t-$CeZrO_4$ polymorph ($P4_2/nmc$). (c) Polymorph composition chart of c-$CeZrO_4$ and t-$CeZrO_4$ in $CeZrO_{4-x}$ samples (x = 0, 300, 600, 900, S, Q). High-resolution X-ray photoelectron spectroscopy (XPS) spectra of the elements (d) Ce, (e) O in $CeZrO_{4-x}$. (f) Ce L_3-edge and (g) Zr K-edge for $CeZrO_4$ and $CeZrO_4$-600 and reference samples. (h) The k^3-weighted Fourier transform spectra of the Zr K-edge in R space. (i) Wavelet transform contour plots of Zr for $CeZrO_4$ and $CeZrO_4$-600.

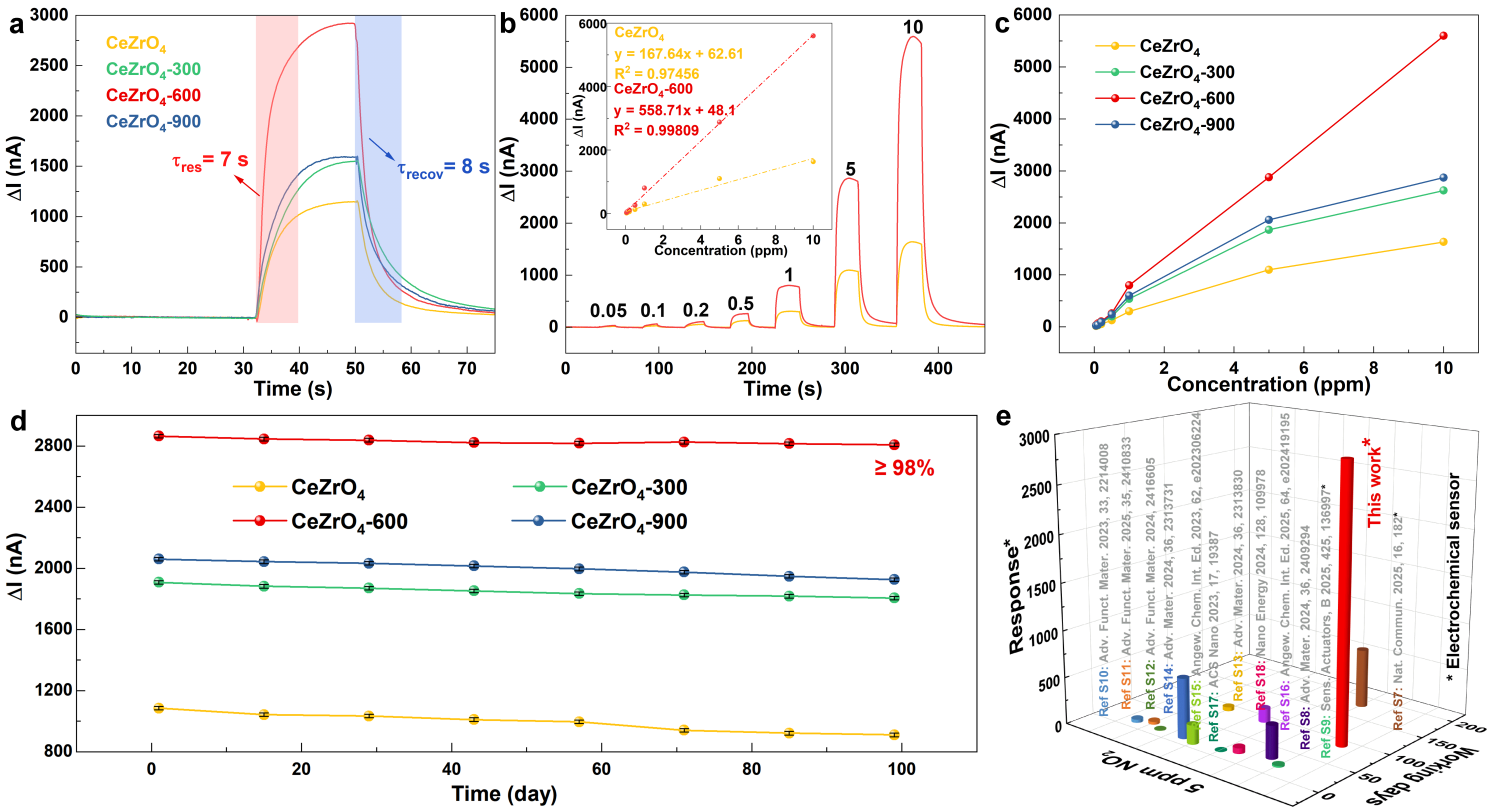


Figure 2

(a) The response current transients of sensors to 5 ppm NO_2 at room temperature. (b) Continuous response and recovery curves to NO_2 in the range of 0.05–10 ppm. The inset shows the linear fit between response current and NO_2 concentration for $CeZrO_4$ and $CeZrO_4$-600. (c) The specific response current variations of the device at different NO_2 concentrations (0.05, 0.1, 0.2, 0.5, 1, 5, 10 ppm). (d) Long-term stability test of $CeZrO_{4-x}$ (x = 300, 600, 900). (e) Comparison of the long-term stability and response values of $CeZrO_4$-600 sensors with those of advanced NO_2 gas sensors reported in the literature.

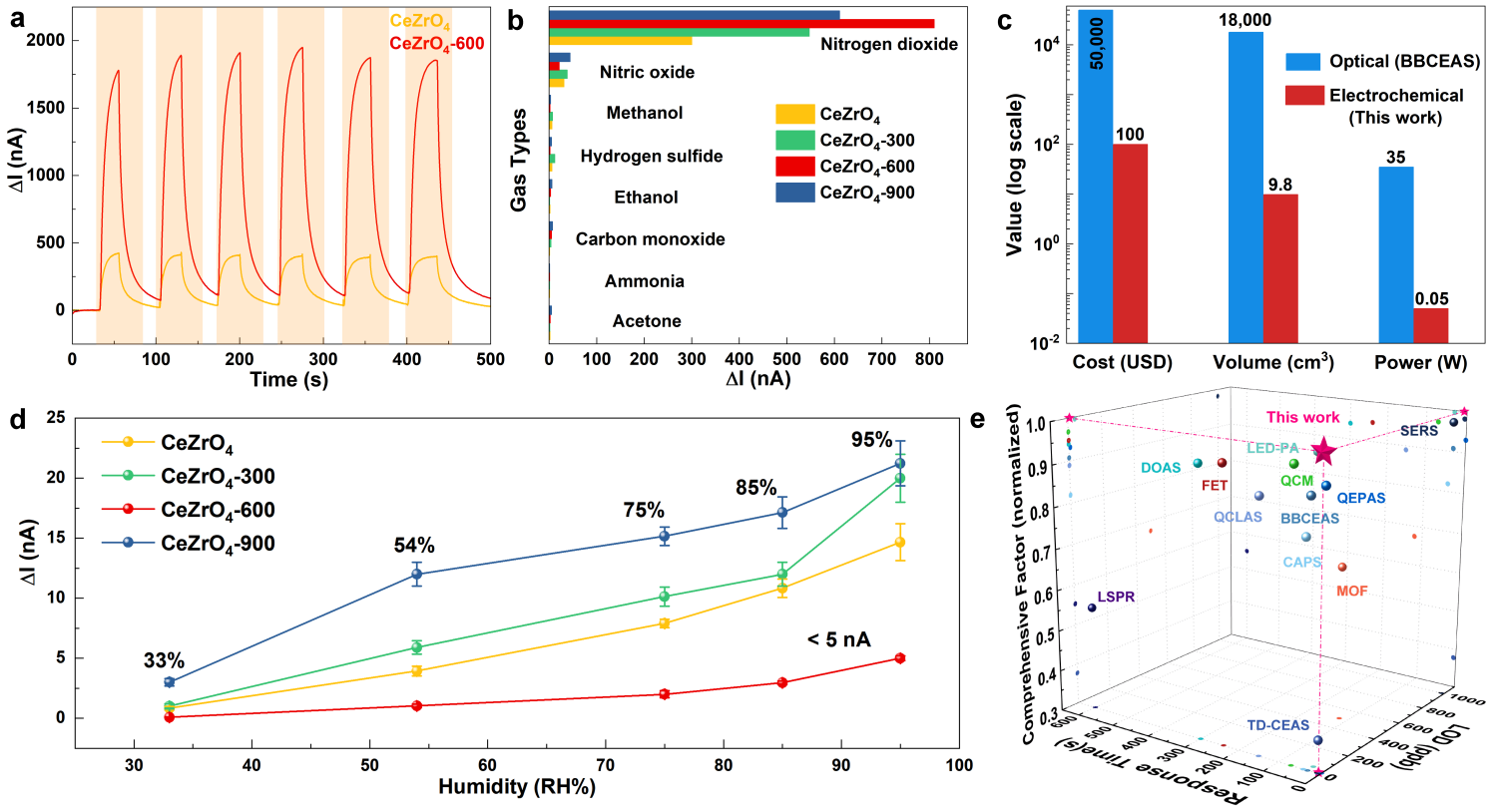


Figure 3

(a) 6-cycle dynamic sensing response current of $CeZrO_4$ and $CeZrO_4$-600 to 3 ppm NO_2. (b) Selectivity of $CeZrO_4$ and $CeZrO_4$-$_x$ (x = 300, 600, 900) sensors for various analytical gases. (c) Comparative overview of optical (BBCEAS) and electrochemical NO_2 sensors in terms of cost, size, and power consumption. (d) Response current of each sensor under varying relative humidity (RH). (e) Performance comparison of reported NO_2 gas sensors across different application fields.

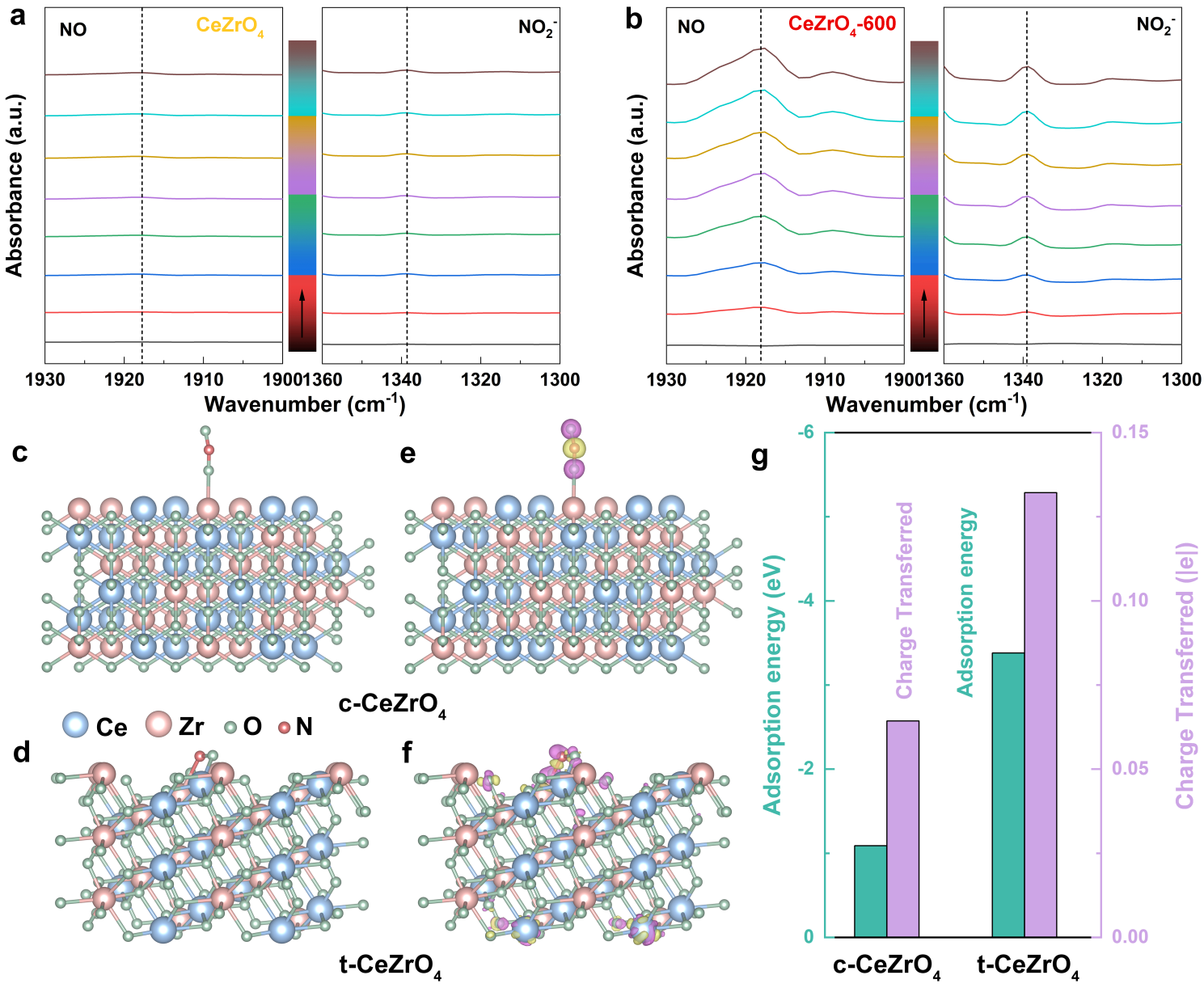


Figure 4

In situ infrared (in situ IR) localized magnification spectroscopy for (a) $CeZrO_4$ and (b) $CeZrO_4$-600 at 5 ppm NO_2, acquired at different time intervals. Representation of molecule structures of NO_2 adsorption on (c) c-$CeZrO_4$ and (d) t-$CeZrO_4$ surfaces. Differential charge density plots of (e) c-$CeZrO_4$ and (f) t-$CeZrO_4$, with yellow and pink regions indicating charge increases and decreases, respectively. (g) Adsorption energies and electron transfer of c-$CeZrO_4$ and t-$CeZrO_4$ to NO_2.

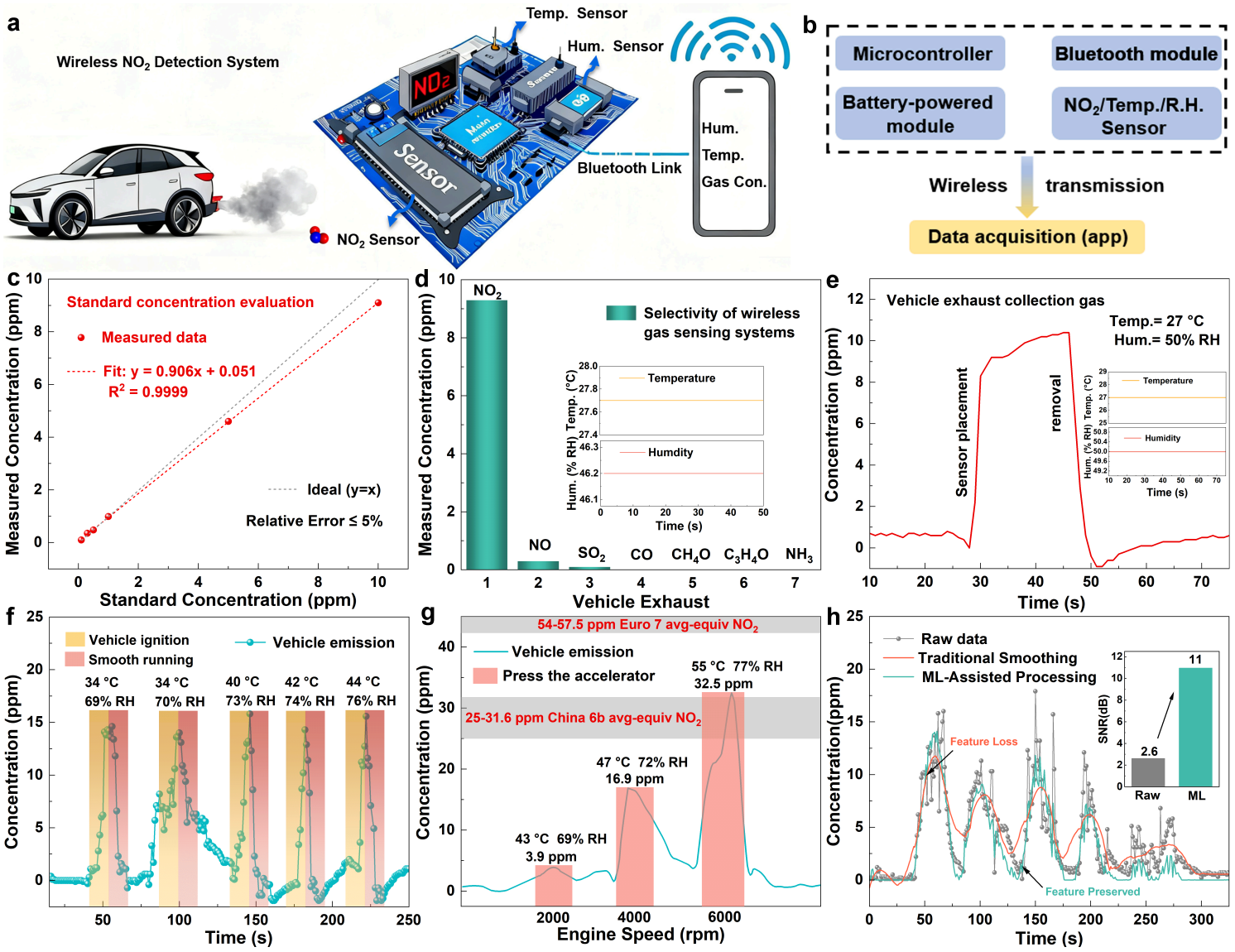


Figure 5

(a) Schematic illustration of the wireless NO_2 detection system based on the $CeZrO_4$-600 sensor. (b) Circuit hardware logic diagram of the wireless NO_2 detection system. (c) Calibration curve of the wireless $CeZrO_4$-600–based system for NO_2 detection over concentrations ranging from 0.1 to 10 ppm. (d) Comparative responses of the NO_2 sensing system to interfering gases present in automobile exhaust. (e) NO_2 detection in collected vehicle exhaust using the wireless sensing system. (f) Real-time exhaust profiles recorded during five consecutive vehicle startups. (g) Real-time exhaust measurements at three different revolutions per minute (rpm). (h) Machine learning (ML) processing improves the signal-to-noise ratio (SNR) of exhaust gas measurements, enhancing NO_2 detection accuracy.

Supplementary Files

This is a list of supplementary files associated with this preprint. Click to download.

- SupplementaryInformation.docx
- VideoS2.mp4
- VideoS1.mp4
- floatimage6.jpeg